Science
AAAS

Two-dimensional diboron trioxide crystal composed by boroxol groups

Authors: T. Zio[1,2]†, M Dirindin[2]†, C. Di Giorgio[1], M. Thaler[3], B. Achatz[3], C. Cepek[1], I Cojocariu[2,4], M. Jugovac[4], T. O. Menteş[4], A. Locatelli[4], L. L. Patera[3], A. Sala[1]*, G. Comelli[1,2], M. Peressi[2]*, C. Africh[1]

Affiliations:

[1]CNR – Istituto Officina dei Materiali (IOM); Basovizza, Trieste, 34149 Italy.

[2]Department of Physics, University of Trieste; Trieste, 34127 Italy.

[3]Department of Physical Chemistry, University of Innsbruck, Innsbruck, 6020 Austria

[4]Elettra Sincrotrone Trieste S.C.p.A; Basovizza, Trieste, 34149 Italy.

*Corresponding author. Email: sala@iom.cnr.it (experiment), peressi@units.it (theory).

†These authors contributed equally to this work.

Abstract: Diboron trioxide (B_2O_3) represents an unusual case among polymorphic oxides, for its vitrified state features superstructural units – planar boroxol groups – that are never observed in its three-dimensional crystalline polymorphs. Crystalline polymorphs that incorporate boroxol groups have only been predicted theoretically, although their formation is crucial to rationalize the ability of B_2O_3 to vitrify. Here we present the synthesis of a two-dimensional crystalline B_2O_3 polymorph constituted by boroxol groups arranged in an atomically thin honeycomb lattice. By combining surface science experimental techniques with ab initio calculations, we characterize the structural and electronic properties of this B_2O_3 polymorph down to the atomic level. This discovery enlarges the family of two-dimensional materials and enables the atomic tracking of individual structural units in trioxides.

DOI: 10.1126/science.adv2582

https://www.science.org/doi/10.1126/science.adv2582

Ultrathin two-dimensional (2D) materials can exhibit complementary properties and functionalities (*1–4*). Among them, the family of 2D oxides (M_xO_y, where M is a metal or metalloid atom) has been extensively investigated for their photovoltaic, sensing and optoelectronic properties that can differ from those of their bulk counterparts (*5*). The experimental realization of atomically thin sheets of silicon dioxide (silica, SiO_2) has also opened new perspectives in the study of polymorphic oxides with atomic resolution (*6*, *7*) and provided insights into the fundamental atomic scale physics behind crystalline-vitreous transitions.

Specifically, by studying at the atomic scale the monolayer and bilayer silica, as a model system for metalloid MO_2, it was demonstrated that the crystalline and vitreous phases of both the 2D and 3D forms of SiO_2 possess the same tetrahedral [$SiØ_4$](*8*) building blocks (*9–15*). The 2D allotrope was exploited to overcome the limitation of tracking individual atoms that generally affects 3D systems. For example, using aberration-corrected transmission electron microscopy, Huang et. al. (*16*) imaged the atomic rearrangement during elastic and plastic deformation, allowing correlations to be made with bulk thermodynamic properties.

Despite these results, atomic-scale information on the two other main classes of polymorphic oxides, M_2O_3 and M_2O_5, has been lacking (*17*). Among the former, diboron trioxide (boria, B_2O_3) represents a peculiar case. On one hand, macroscopic crystallization of boria occurs only under applied pressure, an effect known as crystallization anomaly (*18*, *19*). On the other hand, questions arise on its herein called "apparent vitrification anomaly". Not only its two known crystalline phases, B_2O_3-I and B_2O_3-II, are possibly made of two different building blocks – regular chains of corner-linked [$BØ_3$] triangles (*20*) in B_2O_3-I, and [$BØ_4$] tetrahedra (*21*) in B_2O_3-II – but, even more surprisingly, its vitreous phase shows the presence of yet another structural unit, the so called boroxol [$B_3O_3Ø_3$] group (*22*, *23*). This unit have a notably favorable stabilization energy (–26.8 kJ/mol) (*24*). Since the B_2O_3-I phase formation occurs under pressure, Wright (*25*) raises the question of whether B_2O_3-I is truly the most stable ambient-pressure polymorph or another stable ambient pressure B_2O_3 crystalline polymorph based on boroxol groups might exist.

Ferlat et al. (*26*) offered a tentative rationalization of this complex scenario and predicted through ab-initio calculations the existence of previously unknown microporous crystalline B_2O_3 polymorphs, likely to be also the best model candidates for describing the crystalline nanodomains detected in glassy B_2O_3 by nuclear magnetic resonance (*22*). Among the modelled polymorphs, those with the lowest cohesion enthalpy are all based on 2D and 3D connected networks of boroxol groups. These findings seem to solve the question raised by Wright ~~apparent vitrification anomaly observed in boria~~, but this explanation has not yet been verified experimentally.

We now report experimental evidence of a two-dimensional B_2O_3 crystalline polymorph, synthesized on a Pt(111) substrate and composed exclusively by boroxol groups arranged in a honeycomb lattice. New ab-initio calculations allow the model proposed by Ferlat et al. (*26*) to be validated and refined. Through a detailed joint experimental and theoretical structural characterization, we demonstrate that 2D boria is an innovative atomically thin material with intriguing structural properties, including regular nanoporosity over the mesoscopic scale, strain-tunable pore size, and minimal interaction with the support.

Synthesis and structural characterization

The 2D B_2O_3 layer was obtained through thermal-driven assembly of the B and O atomic constituents on the Pt(111) surface. We used two equivalent growth methods. One was the

deposition of B atoms in ultrahigh vacuum (UHV) and subsequent exposure to O_2 at a substrate temperature of 770 K (left to right in Fig. 1). The other was the deposition of B atoms in oxygen atmosphere also at 770 K (right to left in Fig. 1). Heating the substrate at 770 K was crucial to catalytically split O_2 molecule and to segregate the bulk-dissolved B atoms to the surface, resulting in boron oxidation. In both cases, a final flash annealing at 820 K in UHV was required to complete the growth of crystalline 2D B_2O_3. This last thermal step induced the assembly of the oxidized boron into boroxol groups, which then arranged themselves into the crystalline monolayer. Both growth methods led to the same final structure, and we present the experimental data regardless of the preparation route.

A large-scale scanning tunneling microscopy (STM) image of the B_2O_3 monolayer (Fig. 2A) revealed a honeycomb structure with high degree of crystallinity, where only few defects, appearing as brighter spots and ~~tentatively assigned to molecular adsorbates~~ most likely due to Pt atoms caged in the B_2O_3 network (see Supplemental Information, Fig S1), were present over a surface area of 50 nm by 50 nm. The high-resolution STM image on the bottom right-hand corner of Fig. 2A shows the details of the honeycomb structure, together with an antiphase domain boundary oriented along the armchair direction (dashed line).

STM imaging over large areas detected a variety of rotational domains and moiré patterns (see Supplemental information, Fig. S2), suggesting that boria did not adopt any specific spatial superposition with the substrate atoms. Fig. 2B displays the microspot low-energy electron diffraction (μLEED) hexagonal pattern obtained from a single specific B_2O_3 rotational domain. The corresponding reciprocal space vectors, depicted in blue, are rotated by ~ 30° with respect to the Pt(111) vectors, in green. Both STM and LEED agree on a measured 2D boria lattice constant (distance between two adjacent pores) of 8.57±0.03 Å. The zoomed-in LEED image around the (0;0) beam shows that the 2D boria diffraction spots are surrounded by six weaker satellites as part of one of the possible moiré patterns originating from the superposition of the atomic arrangements of Pt substrate and 2D boria.

The 2D boria stoichiometry was investigated with near-edge x-ray absorption fine structure (NEXAFS) and x-ray photoemission spectroscopy (XPS). The NEXAFS spectrum at the B K-edge (Fig. 2C, upper panel) revealed a single peak at a photon energy of 194.4 eV, in perfect agreement with experimental and calculated values for B^{3+} atoms connected to three O centers, occurring in condensed trinaphtylboroxine molecules on Au(111) (*27*). The photoemission spectra of B 1s and O 1s core-level electrons (Fig. 2C, lower panels) showed peaks at binding energies (BE) of 192.0 eV and 531.8 eV, respectively. The B/O ratio extracted from the 1s peak areas was 0.60±0.15, after correction for the relative photon flux, the photoionization cross section (*28*) and the energy-dependent instrumental efficiency. This value was consistent with B_2O_3 stoichiometry and excluded other crystalline networks, characterized by unitary B/O ratio, theoretically considered previously (*29*).

Theoretical studies

We used density functional theory (DFT) to determine the exact atomic structure of the boria monolayer. We initially neglected the substrate and focused on the free-standing monolayer. The proposed atomic model was made of B_3O_3 hexagonal rings connected by additional O atoms, that is, boroxol $B_3O_3Ø_3$ groups (Fig. 2D(i)) sharing the outermost common oxygen atoms. The centers of the boroxol groups were arranged in a honeycomb structure, with a unit cell containing two of them. All the B-O bond lengths were equal.

In the first ("rigid") version of the model, the angle θ between neighboring groups was fixed at 180° (Fig. 2D(ii)). The resulting equilibrium DFT lattice parameter was 9.52 Å, much larger than the experimentally determined value, with the B-O bond length equal to 1.375 Å. If θ was reduced to 120°, the structure became the T0-b polymorph predicted by Ferlat et al. (*26*), which features triangular pores (Fig. 2D(iii)), resembling those observed in our ~~high-resolution~~ STM images but with a predicted lattice parameter of 8.25 Å now smaller than the experimental one.

We thus refined the model by allowing θ to vary, while keeping rigid the internal structure of the $B_3O_3Ø_3$ groups ("flexible" model). Fig. 2~~C~~D(iv) summarizes our DFT results, displaying the total energy per atom as a function of the lattice parameter (upper axis) or strain (lower axis) for (i) the rigid model where θ is fixed at 180° but the B-O bond lengths are equally rescaled (red curve) and (ii) the flexible model where θ varies but the B-O bond length is fixed to 1.375 Å, that is, the equilibrium value in the "rigid" model (blue curve).

In the simulated strain range, the flexible model is overall energetically favoured, resulting in an equilibrium configuration with θ = 136.9° and a lattice parameter of 8.86 Å, slightly closer to the experimental value. The residual discrepancy between the two values may be attributed to the exclusion of the substrate in the calculations. This configuration is also clearly favored with respect to the θ = 120° one (T0-b model) by about 50 meV/atom, well beyond our numerical accuracy.

From the energy-strain relationship, the isotropic strain was calculated (*30*, *31*), resulting in a stiffness of ~ 30 Pa*m for the flexible model. This value was remarkably small compared to the 2D Young's modulus of graphene (~ 340 Pa*m (*31–33*)) and h-BN (~ 280 Pa*m (*34*, *35*)), pointing to 2D B_2O_3 as the softest one-atom-thick material reported so far, one order of magnitude softer than graphene. The stiffness is comparable to some thicker 2D materials, such as black phosphorus (20 to 50 Pa*m) and transition-metal dichalcogenides (110 Pa*m for WSe_2 and $MoSe_2$) (*36*).

Besides the atomic model constituted solely by boroxol rings, we employed DFT to study alternative 2D B_2O_3 polymorphs proposed in previous theoretical work (*37*). Such models also incorporate $BØ_3$ triangles on the basis of the generally accepted idea that borate glasses (and possibly the crystalline nanodomains herein) consist of a network of independent BO_3 triangles and boroxol groups (*38*). Based on the large mismatch between measured and calculated lattice constants and the different STM appearance, we can rule out those models (see Supplemental Information, Fig. S3).

We investigated in more detail the 2D boroxol-based polymorph by including the Pt(111) substrate in the DFT calculation, now focusing our attention on the boria-substrate interaction and on the resulting overall band structure. The computational model was set up starting from the Pt(111) lattice parameter and the observed 2D B_2O_3 periodicity. We emphasize that this periodicity was indeed the fundamental criterion to set the model, while the relative orientation of substrate, overlayer and moiré was not relevant for a comparison with the experimental data and could be different with respect to the specific domain experimentally examined here.

We considered different misorientation angles and strain conditions of the overlayer, identifying a set of 2D coincidence cells of reasonable sizes. Guided by the experimental data, we selected within this set the smallest 2D supercell, shown in top and side views in Fig. 3A. It is a hexagonal cell with 67 Pt atoms per layer and 14 boroxol groups (306 atoms in total considering the 3-layer Pt slab) and an in-plane lattice parameter of 22.79 Å, corresponding to a 2D B_2O_3 lattice parameter of 8.61 Å, very near the experimental value. The misorientation angle between

substrate and boria lattice vectors was about 7°. The moiré supercell was rotated by about 20° with respect to the boria lattice vectors and by about 13° with respect to the Pt(111) surface lattice vectors.

The optimization of the atomic positions in this structure gives a rather flat configuration of the boria layer (buckled by 0.2 Å only), with an angle θ = 127.8° between neighboring boroxol groups and an average distance of 3.26 Å from the substrate, comparable to the one adopted by graphene on Pt(111) (*39*). Fig. 3B compares the proposed model with a topographic STM image and a dI/dV conductance map acquired in constant-height mode and Laplace filtered. In the latter, oxygen atoms are seen as bright protrusions, as for the case of bilayer SiO_2 (*10*). The comparison is completed by STM simulation, obtained by Tersoff-Hamann rendering of the DFT calculation of the relaxed model, smoothed by a mild Gaussian broadening. The agreement is remarkable — not only in the appearance of the boroxol groups, unresolved by topographic STM, but clearly visible in dI/dV — but also in the triangular shape of the ~ 5 Å wide pores.

Electronic band structure

The monolayer-substrate distance obtained by the DFT calculations suggested a very weak interaction of boria with the substrate. This result was corroborated by the analysis of the electronic density of states (DOS) projected on the boria layer (Fig. 3C, red curve), which was almost perfectly matching that of the free-standing case (blue curve). The details of the band structure of the boria layer could be conveniently studied using the free-standing layer, as shown in the left panel of Fig. 3C along high symmetry directions in the primitive cell. We note that the calculated band structure yields an indirect bandgap of 6.2 eV. The occupied states present a strong superposition of bands with low dispersion near the Fermi energy, with the related electronic states mainly localized at the oxygen atoms (see Supplemental information – Fig. S4). Bands at lower energy present instead a larger dispersion.

~~Photoemission Spectroscopy~~

To validate the calculated band structure of 2D boria with experimental data, we applied angle-resolved photoemission spectroscopy (ARPES). Fig. 3D compares the experimental momentum distribution curve, measured along the high symmetry axes of the Pt(111) First Brillouin Zone (FBZ), and the calculated band structure of B_2O_3 unfolded into the same FBZ (*40*). The binding energy in the calculated plot was shifted to match the experimental data. Inside the bandgap of 2D boria, the Pt(111) band structure was still visible in the experimental data, although damped in intensity by the presence of the boria overlayer.

The agreement between the calculated and experimental band structures was remarkable, both for the bands in the low-dispersion region between 5 and 7 eV BE and for those with larger dispersion at around 9 eV BE. Such matching strongly confirmed the validity of the results we have obtained for Pt(111) supported boria, concerning the structural model, the electronic structure and the related properties. For completeness, ARPES maps taken on k_x-k_y plane at selected BEs of the 2D boria bands are presented in the Supplemental information (Fig. S5).

Concerning the electron density distribution in real space, both the projected Löwdin charges and the plots of the differential electron density distribution, that is, the difference between the distribution in the total system and the sum of the distribution in the two constituting systems (free-standing boria and Pt(111) slab) - indicate that there is no appreciable charge transfer between substrate and overlayer. Indeed, the differential electron density distribution along the hexagonal motif displayed in Fig. 3E shows only a small polarization occurring at the interface.

Adlayer adhesion

From DFT calculations, we could also evaluate the adhesion energy of the overlayer, defined as the difference between the total energy of the entire system and the sum of the two separate constituents, obtaining a rather small value, further supporting a weak interaction with the substrate:

$$E_{\cancel{ads}adh} = -0.41 \frac{eV}{B_2O_3\ formula\ unit} = -0.019\ eV/Å^2.$$

Interestingly, the boria adhesion energy on Pt(111) was intermediate between those of 2D germania (-0.022 eV/Å^2) and silica (-0.013 eV/Å^2) bilayers on the same substrate (*41*), with the latter capable of withstanding mechanical exfoliation from a Ru(0001) substrate (adhesion energy -0.018 eV/Å^2) and transfer to a new support (*42*). Finally, the weak interaction between boria and the Pt substrate is indirectly confirmed by the abundance of rotational domains and moiré patterns with modest height corrugation (less than 0.1 Å) that were detected in STM experiments (see Supplemental information – Fig. S2), a hallmark of systems with minimal interfacial coupling. Similar behavior has been reported for graphene on Ir(111) (*43*) and Pt(111) (*39*), where the coexistence of multi-oriented moiré superstructures and the lack of a preferred orientation are attributed to weak substrate coupling.

Discussion

We synthesized 2D boria and provided experimental and theoretical evidence of the existence of the most elemental B_2O_3 polymorph, composed of boroxol groups arranged in a large-scale ordered honeycomb structure.~~, confirming and refining the theoretical prediction of Ferlat et al. (*22*).~~ In doing so, we have not only confirmed and refined the prediction of Ferlat et al. (*26*), but also addressed the long-standing question posed by Wright (*24*, *25*) of whether a stable, ambient-pressure crystalline B_2O_3 polymorph based on boroxol unit blocks may exist. The exclusive presence of boroxol groups in the 2D network, confirmed by the theoretical calculations, is direct evidence that their formation is energetically favored over the separated synthesis of more elemental [BØ$_3$] triangles in low-pressure conditions, even if confined in a 2D frame. The reliability of the calculated atomic model is supported not only by its excellent agreement with the dI/dV conductance map and the experimental lattice constant, but also by its ability to reproduce key features of the experimental electronic band structure.

Experimental measurements using STM, LEED, XPS, NEXAFS and ARPES, as well as complementary ab initio calculations, demonstrate that this material has several intriguing properties. The boroxol 2D network is nanoporous by construction and constitutes the inorganic rendition of 2D polyphenylene (*44*), with the difference that the covalent bonding between benzene rings is now replaced by oxygen atoms bridging B_3O_3 rings. This peculiar linker gives the structure a remarkable mechanical softness – the calculated isotropic stress tensor is one order of magnitude lower than graphene – enabling possible tuning of the nanopore size by tensile strain. Moreover, the fabricated 2D boria can cover most of the substrate surface with a mosaic of rotational domains that extend over highly ordered areas of tens of square micrometers, with negligible defect density. We used ab initio numerical simulations to demonstrate that the electronic interaction between the Pt substrate and the 2D boria network was very weak, quantitatively comparable to that occurring between 2D bilayer silica and the same substrate. This finding suggests the possibility of transferring the 2D film to other substrates for applications.

The synthesis of a boroxine-based 2D crystalline form of boria permits to review some of the key findings on the atomic structure of borate materials, in both crystalline and vitreous form. It is

widely accepted that in glasses the relative abundance ratio between $B\O_3$ and $B_3O_3\O_3$ structural units is roughly 1:1 (*38*). Therefore, considerable effort has been made to figure out possible crystalline structures of such composition that may describe the crystalline nanodomains detected in the vitreous phase. The evidence we provide for the existence of a pure boroxol 2D phase does not exclude that other crystalline structures that incorporate $B\O_3$ may exist. On the contrary, the support-aided growth protocol described here could be exploited to tentatively create other predicted allotropic forms by systematically exploring different preparation conditions. The boroxine-based 2D structure could also constitute the base of a layered 3D structure, as it occurs for the crystalline phase of its sulphur analogue, B_2S_3 (*24*), and for more complex boron compounds such as borosulphates, which are made of alternate layers of boron oxide and alkali sulphate-hydrogensulphate (*45*). Moreover, the synthesis of 2D boria makes it possible to extend the investigation of the crystalline-vitreous transition with atomic resolution to the M_2O_3 case, as happened for 2D SiO_2, and to characterize at the atomic scale the breaking up and reformation of boroxol groups into triangular units upon thermal annealing. This last aspect is particularly important, as the structure of (supercooled) liquid B_2O_3 is dominated not only by the usual cybotactic groupings, but also by the thermally driven dynamical equilibrium between $B_3O_3\O_3$ groups and $B\O_3$ triangles.

References and Notes

1. A. K. Geim, K. S. Novoselov, The rise of graphene. *Nature Mater.* **6**, 183–191 (2007).

2. A. C. Ferrari, F. Bonaccorso, V. Fal'ko, K. S. Novoselov, S. Roche, P. Bøggild, S. Borini, F. H. L. Koppens, V. Palermo, N. Pugno, J. A. Garrido, R. Sordan, A. Bianco, L. Ballerini, M. Prato, E. Lidorikis, J. Kivioja, C. Marinelli, T. Ryhänen, A. Morpurgo, J. N. Coleman, V. Nicolosi, L. Colombo, A. Fert, M. Garcia-Hernandez, A. Bachtold, G. F. Schneider, F. Guinea, C. Dekker, M. Barbone, Z. Sun, C. Galiotis, A. N. Grigorenko, G. Konstantatos, A. Kis, M. Katsnelson, L. Vandersypen, A. Loiseau, V. Morandi, D. Neumaier, E. Treossi, V. Pellegrini, M. Polini, A. Tredicucci, G. M. Williams, B. Hee Hong, J.-H. Ahn, J. Min Kim, H. Zirath, B. J. van Wees, H. van der Zant, L. Occhipinti, A. Di Matteo, I. A. Kinloch, T. Seyller, E. Quesnel, X. Feng, K. Teo, N. Rupesinghe, P. Hakonen, S. R. T. Neil, Q. Tannock, T. Löfwander, J. Kinaret, Science and technology roadmap for graphene, related two-dimensional crystals, and hybrid systems. *Nanoscale* **7**, 4598–4810 (2015).

3. M. Naguib, V. N. Mochalin, M. W. Barsoum, Y. Gogotsi, 25th Anniversary Article: MXenes: A New Family of Two-Dimensional Materials. *Adv. Mater.* **26**, 992–1005 (2014).

4. A. Castellanos-Gomez, Why all the fuss about 2D semiconductors? *Nature Photon.* **10**, 202–204 (2016).

5. K. Zhou, G. Shang, H.-H. Hsu, S.-T. Han, V. A. L. Roy, Y. Zhou, Emerging 2D Metal Oxides: From Synthesis to Device Integration. *Adv. Mater.* **35**, 2207774 (2023).

6. C. Büchner, M. Heyde, Two-dimensional silica opens new perspectives. *Prog. Surf. Sci.* **92**, 341–374 (2017).

7. J. Q. Zhong, H. J. Freund, Two-Dimensional Ultrathin Silica Films. *Chem. Rev.* **122**, 11172–11246 (2022).

8. In the following, we represent bridging oxygen atoms between two (super)structural units as Ø, and oxygen atoms within a unit as O.

9. D. Löffler, J. J. Uhlrich, M. Baron, B. Yang, X. Yu, L. Lichtenstein, L. Heinke, C. Büchner, M. Heyde, S. Shaikhutdinov, H.-J. Freund, R. Włodarczyk, M. Sierka, J. Sauer, Growth and Structure of Crystalline Silica Sheet on Ru(0001). *Phys. Rev. Lett.* **105**, 146104 (2010).

10. L. Lichtenstein, C. Büchner, B. Yang, S. Shaikhutdinov, M. Heyde, M. Sierka, R. Włodarczyk, J. Sauer, H.-J. Freund, The atomic structure of a metal-supported vitreous thin silica film. *Angew. Chem. Int. Ed. Engl.* **51**, 404–7 (2012).

11. P. Y. Huang, S. Kurasch, A. Srivastava, V. Skakalova, J. Kotakoski, A. V. Krasheninnikov, R. Hovden, Q. Mao, J. C. Meyer, J. Smet, D. A. Muller, U. Kaiser, Direct imaging of a two-dimensional silica glass on graphene. *Nano Lett.* **12**, 1081–6 (2012).

12. S. Shaikhutdinov, H.-J. Freund, Ultrathin Silica Films on Metals: The Long and Winding Road to Understanding the Atomic Structure. *Adv. Mater.* **25**, 49–67 (2013).

13. P. J. Heaney, Structure and Chemistry of the Low-Pressure Silica Polymorphs. *Rev. Mineral. Geochem.* **29**, 1–40 (1994).

14. C. H. L. Goodman, Strained mixed-cluster model for glass structure. *Nature* **257**, 370–372 (1975).

15. R. Wang, M. D. Merz, Non-crystallinity and polymorphism in elemental solids. *Nature* **260**, 35–36 (1976).

16. P. Y. Huang, S. Kurasch, J. S. Alden, A. Shekhawat, A. A. Alemi, P. L. McEuen, J. P. Sethna, U. Kaiser, D. A. Muller, Imaging Atomic Rearrangements in Two-Dimensional Silica Glass: Watching Silica's Dance. *Science* **342**, 224–227 (2013).

17. W. H. Zachariasen, The Atomic Arrangement In Glass. *J. Am. Chem. Soc.* **54**, 3841–3851 (1932).

18. Uhlmann, Donald Robert and Hays, JF and Turnbull, David, *The Effect of High Pressure on B_2O_3: Crystallization, Densification and the Crystallization Anomaly* (Division of Engineering and Applied Physics, Harvard University, 1966).

19. M. J. Aziz, E. Nygren, J. F. Hays, D. Turnbull, Crystal growth kinetics of boron oxide under pressure. *J. Appl. Phys.* **57**, 2233–2242 (1985).

20. G. E. Gurr, P. W. Montgomery, C. D. Knutson, B. T. Gorres, The crystal structure of trigonal diboron trioxide. *Acta Cryst. B* **26**, 906–915 (1970).

21. C. T. Prewitt, R. D. Shannon, Crystal structure of a high-pressure form of B_2O_3. *Acta Cryst. B* **24**, 869–874 (1968).

22. R. E. Youngman, S. T. Haubrich, J. W. Zwanziger, M. T. Janicke, B. F. Chmelka, Short- and Intermediate-Range Structural Ordering in Glassy Boron Oxide. *Science* **269**, 1416–1420 (1995).

23. G. Ferlat, T. Charpentier, A. P. Seitsonen, A. Takada, M. Lazzeri, L. Cormier, G. Calas, F. Mauri, Boroxol Rings in Liquid and Vitreous B_2O_3 from First Principles. *Phys. Rev. Lett.* **101**, 065504 (2008).

24. Adrian C. Wright, The structural chemistry of B_2O_3. *Phys. Chem. Glass.* **59**, 65–87 (2018).

25. A. C. Wright, My Borate Life: An Enigmatic Journey. *Int. J. Appl. Glass Sci.* **6**, 45–63 (2015).

26. G. Ferlat, A. P. Seitsonen, M. Lazzeri, F. Mauri, Hidden polymorphs drive vitrification in B_2O_3. *Nature Mater.* **11**, 925–929 (2012).

27. D. Toffoli, E. Turco, M. Stredansky, R. Costantini, M. Dell'Angela, L. Floreano, A. Goldoni, A. Morgante, G. Kladnik, D. Cvetko, D. G. de Oteyza, L. Colazzo, M. S. G. Mohammed, A. Sala, G. Comelli, C. Africh, G. Fronzoni, G. Balducci, M. Stener, H. Ustunel, A. Cossaro, Oxygen-Promoted on-Surface Synthesis of Polyboroxine Molecules. *Chem. Eur. J.* **30**, e202401565 (2024).

28. J. J. Yeh, I. Lindau, Atomic subshell photoionization cross sections and asymmetry parameters: 1<Z<103. *Atomic Data and Nuclear Data Tables* **32**, 1–155 (1985).

29. S. Ullah, P. A. Denis, F. Sato, Theoretical investigation of various aspects of two dimensional holey boroxine, B_3O_3. *RSC Advances* **9**, 37526–37536 (2019).

30. Y. Huang, J. Wu, K. C. Hwang, Thickness of graphene and single-wall carbon nanotubes. *Phys. Rev. B* **74**, 245413 (2006).

31. F. Memarian, A. Fereidoon, M. Darvish Ganji, Graphene Young's modulus: Molecular mechanics and DFT treatments. *Superlattices Microstruct.* **85**, 348–356 (2015).

32. I. V. Lebedeva, A. S. Minkin, A. M. Popov, A. A. Knizhnik, Elastic constants of graphene: Comparison of empirical potentials and DFT calculations. *Physica E* **108**, 326–338 (2019).

33. C. Lee, X. Wei, J. W. Kysar, J. Hone, Measurement of the Elastic Properties and Intrinsic Strength of Monolayer Graphene. *Science* **321**, 385–388 (2008).

34. K. N. Kudin, G. E. Scuseria, B. I. Yakobson, C_2F, BN, and C nanoshell elasticity from ab initio computations. *Phys. Rev. B* **64**, 235406 (2001).

35. L. Song, L. Ci, H. Lu, P. B. Sorokin, C. Jin, J. Ni, A. G. Kvashnin, D. G. Kvashnin, J. Lou, B. I. Yakobson, P. M. Ajayan, Large Scale Growth and Characterization of Atomic Hexagonal Boron Nitride Layers. *Nano Lett.* **10**, 3209–3215 (2010).

36. C. Androulidakis, K. Zhang, M. Robertson, S. Tawfick, Tailoring the mechanical properties of 2D materials and heterostructures. *2D Mater.* **5**, 032005 (2018).

37. G. Ferlat, M. Hellgren, F.-X. Coudert, H. Hay, F. Mauri, M. Casula, van der Waals forces stabilize low-energy polymorphism in B_2O_3: Implications for the crystallization anomaly. *Phys. Rev. Mater.* **3**, 063603 (2019).

38. P. A. V. Johnson, A. C. Wright, R. N. Sinclair, A neutron diffraction investigation of the structure of vitreous boron trioxide. *J. Non-Cryst. Solids* **50**, 281–311 (1982).

39. P. Sutter, J. T. Sadowski, E. Sutter, Graphene on Pt(111): Growth and substrate interaction. *Phys. Rev. B* **80**, 1–10 (2009).

40. D. Pacilè, C. Cardoso, G. Avvisati, I. Vobornik, C. Mariani, D. A. Leon, P. Bonfà, D. Varsano, A. Ferretti, M. G. Betti, Narrowing of d bands of FeCo layers intercalated under graphene. *Appl. Phys. Lett.* **118**, 121602 (2021).

41. A. L. Lewandowski, S. Tosoni, L. Gura, Z. Yang, A. Fuhrich, M. J. Prieto, T. Schmidt, D. Usvyat, W.-D. Schneider, M. Heyde, G. Pacchioni, H.-J. Freund, Growth and Atomic-Scale Characterization of Ultrathin Silica and Germania Films: The Crucial Role of the Metal Support. *Chem. Eur. J.* **27**, 1870–1885 (2020).

42. C. Büchner, Z.-J. Wang, K. M. Burson, M.-G. Willinger, M. Heyde, R. Schlögl, H.-J. Freund, A Large-Area Transferable Wide Band Gap 2D Silicon Dioxide Layer. *ACS Nano* **10**, 7982–7989 (2016).

43. A. T. N'Diaye, J. Coraux, T. N. Plasa, C. Busse, T. Michely, Structure of epitaxial graphene on Ir(111). *New J. Phys.* **10**, 043033 (2008).

44. M. Bieri, M.-T. Nguyen, O. Gröning, J. Cai, M. Treier, K. Aït-Mansour, P. Ruffieux, C. A. Pignedoli, D. Passerone, M. Kastler, K. Müllen, R. Fasel, Two-Dimensional Polymer Formation on Surfaces: Insight into the Roles of Precursor Mobility and Reactivity. *J. Am. Chem. Soc.* **132**, 16669–16676 (2010).

45. M. Daub, H. Hillebrecht, Borosulfates $Cs_2B_2S_3O_{13}$, $Rb_4B_2S_4O_{17}$, and $A_3HB_4S_2O_{14}$ (A = Rb, Cs) – Crystalline Approximants for Vitreous B_2O_3? *Eur. J. Inorg. Chem.* **2015**, 4176–4181 (2015).

46. G. D. Nguyen, H.-Z. Tsai, A. A. Omrani, T. Marangoni, M. Wu, D. J. Rizzo, G. F. Rodgers, R. R. Cloke, R. A. Durr, Y. Sakai, F. Liou, A. S. Aikawa, J. R. Chelikowsky, S. G. Louie, F. R. Fischer, M. F. Crommie, Atomically precise graphene nanoribbon heterojunctions from a single molecular precursor. *Nature Nanotechnol.* **12**, 1077–1082 (2017).

47. P. H. Jacobse, Z. Jin, J. Jiang, S. Peurifoy, Z. Yue, Z. Wang, D. J. Rizzo, S. G. Louie, C. Nuckolls, M. F. Crommie, Pseudo-atomic orbital behavior in graphene nanoribbons with four-membered rings. *Sci. Adv.* **7**, eabl5892 (2021).

48. K. Sun, O. J. Silveira, Y. Ma, Y. Hasegawa, M. Matsumoto, S. Kera, O. Krejčí, A. S. Foster, S. Kawai, On-surface synthesis of disilabenzene-bridged covalent organic frameworks. *Nat. Chem.* **15**, 136–142 (2023).

49. T. O. Menteş, G. Zamborlini, A. Sala, A. Locatelli, Cathode lens spectromicroscopy: methodology and applications. *Beilstein J. Nanotechnol.* **5**, 1873–86 (2014).

50. A. Sala, "Imaging at the Mesoscale (LEEM, PEEM)" in *Springer Handbook of Surface Science* (Springer, Cham, 2020), pp. 387–425.

51. P. Giannozzi, S. Baroni, N. Bonini, M. Calandra, R. Car, C. Cavazzoni, D. Ceresoli, G. L. Chiarotti, M. Cococcioni, I. Dabo, A. Dal Corso, S. de Gironcoli, S. Fabris, G. Fratesi, R. Gebauer, U. Gerstmann, C. Gougoussis, A. Kokalj, M. Lazzeri, L. Martin-Samos, N. Marzari, F. Mauri, R. Mazzarello, S. Paolini, A. Pasquarello, L. Paulatto, C. Sbraccia, S. Scandolo, G. Sclauzero, A. P. Seitsonen, A. Smogunov, P. Umari, R. M. Wentzcovitch, QUANTUM ESPRESSO: a modular and open-source software project for quantum simulations of materials. *J. Phys.: Condens. Matter* **21**, 395502 (2009).

52. P. Giannozzi, O. Andreussi, T. Brumme, O. Bunau, M. B. Nardelli, M. Calandra, R. Car, C. Cavazzoni, D. Ceresoli, M. Cococcioni, N. Colonna, I. Carnimeo, A. D. Corso, S. de Gironcoli, P. Delugas, R. A. DiStasio, A. Ferretti, A. Floris, G. Fratesi, G. Fugallo, R. Gebauer, U. Gerstmann, F. Giustino, T. Gorni, J. Jia, M. Kawamura, H.-Y. Ko, A. Kokalj, E. Küçükbenli, M. Lazzeri, M. Marsili, N. Marzari, F. Mauri, N. L. Nguyen, H.-V. Nguyen, A. Otero-de-la-Roza, L. Paulatto, S. Poncé, D. Rocca, R. Sabatini, B. Santra, M. Schlipf, A. P. Seitsonen, A. Smogunov, I. Timrov, T. Thonhauser, P. Umari, N. Vast, X. Wu, S. Baroni, Advanced capabilities for materials modelling with Quantum ESPRESSO. *J. Phys.: Condens. Matter* **29**, 465901 (2017).

53. J. P. Perdew, K. Burke, M. Ernzerhof, Generalized Gradient Approximation Made Simple. *Phys. Rev. Lett.* **77**, 3865–3868 (1996).

54. K. F. Garrity, J. W. Bennett, K. M. Rabe, D. Vanderbilt, Pseudopotentials for high-throughput DFT calculations. *Comput. Mater. Sci.* **81**, 446–452 (2014).

55. N. Marzari, D. Vanderbilt, A. De Vita, M. C. Payne, Thermal Contraction and Disordering of the Al(110) Surface. *Phys. Rev. Lett.* **82**, 3296–3299 (1999).

56. S. Grimme, J. Antony, S. Ehrlich, H. Krieg, A consistent and accurate ab initio parametrization of density functional dispersion correction (DFT-D) for the 94 elements H-Pu. *J. Chem. Phys.* **132**, 154104 (2010).

57. unfold-x package; https://bitbucket.org/bonfus/unfold-x.

Acknowledgments: We thank Daniele Coslovich, Antimo Marrazzo, Davide Bidoggia, Albano Cossaro and Hans-Joachim Freund for fruitful discussions, and Sumati Patil and Ayesha Farooq for their contribution to preliminary XPS experiments.

Funding: We acknowledge funding from the project QUBOP within the Progetti di ricerca di Rilevante Interesse Nazionale (PRIN) 2022 initiative, funded by European Union – Next Generation EU, Mission 4 Component 1, CUP J53D23001410006 through MUR — Italian Ministry for Universities and Research, from ICSC – Centro Nazionale di Ricerca in High Performance Computing, Big Data and Quantum Computing, funded by European Union – Next

Generation EU, Mission 4 Component 2 Investment 1.4 CUP J93C22000540006, from National Quantum Science and Technology Institute (NQSTI) grant PE00000023 funded by European Union – Next Generation EU, Mission 4 Component 2 Investment 1.3 CUP J93C22001510006, and from Network 4 Energy Sustainable Transition (NEST) funded by European Union – Next Generation EU, Mission 4 Component 2 Investment 1.3 CUP B53C22004060006. B.A. and L.L.P. acknowledge support from the ERC under the European Union's Horizon 2020 research and innovation programme (grant agreement no. 101039746) funded by the European Union.

Author contributions: Conceptualization: AS, MP; Methodology: AS, MP; Investigation: TZ, MD, CDG, MT, BA, CC, IC, MJ, TOM, AL, LLP, AS, MP; Visualization: TZ, MD, AS, MP; Funding acquisition: AS, LLP, GC, MP, CA; Project administration: AS, MP, CA; Supervision: AS, LLP, GC, MP, CA; Writing – original draft: TZ, MD, AS, MP; Writing – review & editing: all authors.

Competing interests: Authors declare that they have no competing interests.

Data and materials availability: All data are available in the main text or the supplementary materials.

Supplementary Materials

Materials and Methods

Figs. S1 to S5

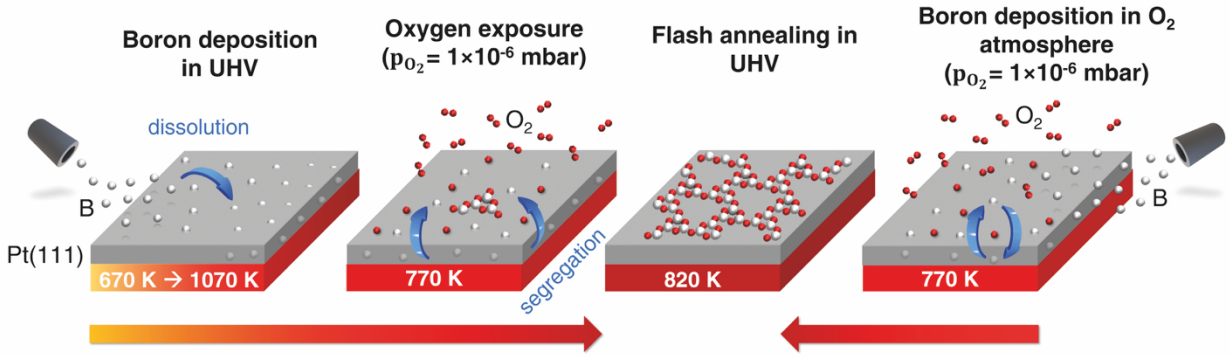

Fig. 1: **Alternative UHV synthesis protocols for 2D B_2O_3 layer on Pt(111).** Boron can be either deposited and subsequently oxidized (left to right) or directly deposited in oxidation conditions (right to left). Both routes, after a final flash annealing in UHV to reorganize the BO_x complexes, result in a crystalline network of boroxol groups.

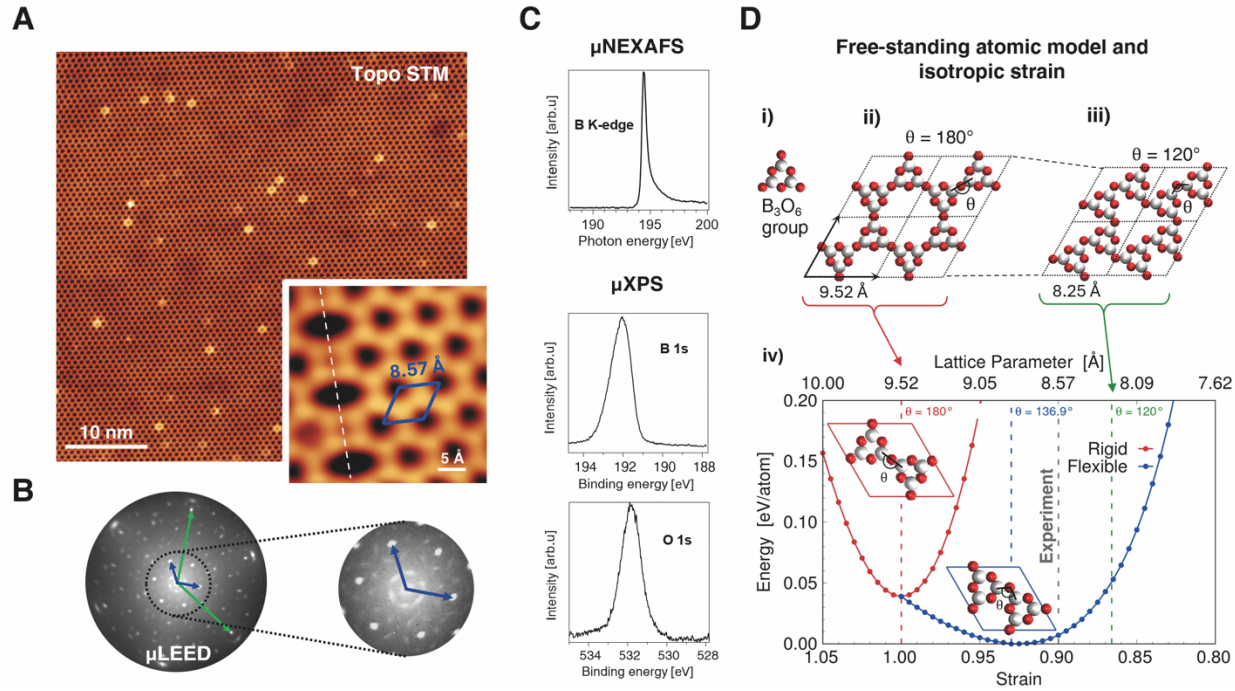

Fig. 2: **Atomic structure and chemical composition of 2D B_2O_3.** (**A**) Topographic STM imaging (0.2 nA, +1.0 V) of the as-prepared sample. The zoom-in image shows the honeycomb lattice (unit cell in blue) and a domain boundary (white dashed line). (**B**) Detected μLEED pattern (with zoomed center), where the Pt(111) and B_2O_3 reciprocal lattice vectors are displayed (green and blue, respectively). (**C**) Top panel: Selected-area NEXAFS spectrum of B K-edge of B_2O_3/Pt(111), showing only one component at 194.4 eV photon energy corresponding to B^{3+} oxidation state. Bottom panels: Selected-area XPS spectra of B 1s and O 1s core levels. (**D**) Atomic models of: (i) boroxol [$B_3O_3Ø_3$] unit (white/red spheres corresponding to B/O atoms, respectively); (ii) and (iii): B_2O_3 structure with rigid boroxol groups in a honeycomb network with (ii) a fixed angle θ = 180° ("rigid" model) and (iii) a varying θ angle ("flexible" model; here θ = 120°) between the boroxol neighboring units; (iv) DFT-calculated total energy per atom as a function of the unit cell strain (bottom axis) / lattice parameter (top axis). The cell strain

corresponds to a homogeneous strain of all the B-O bond lengths in the "rigid" model (red points/curve) and a variation of the angle θ, keeping fixed the B-O bond lengths, in the "flexible" model (blue points/curve). The reference value for the strain is the rigid structure ii), while the reference value for the energy is the flexible optimized structure.

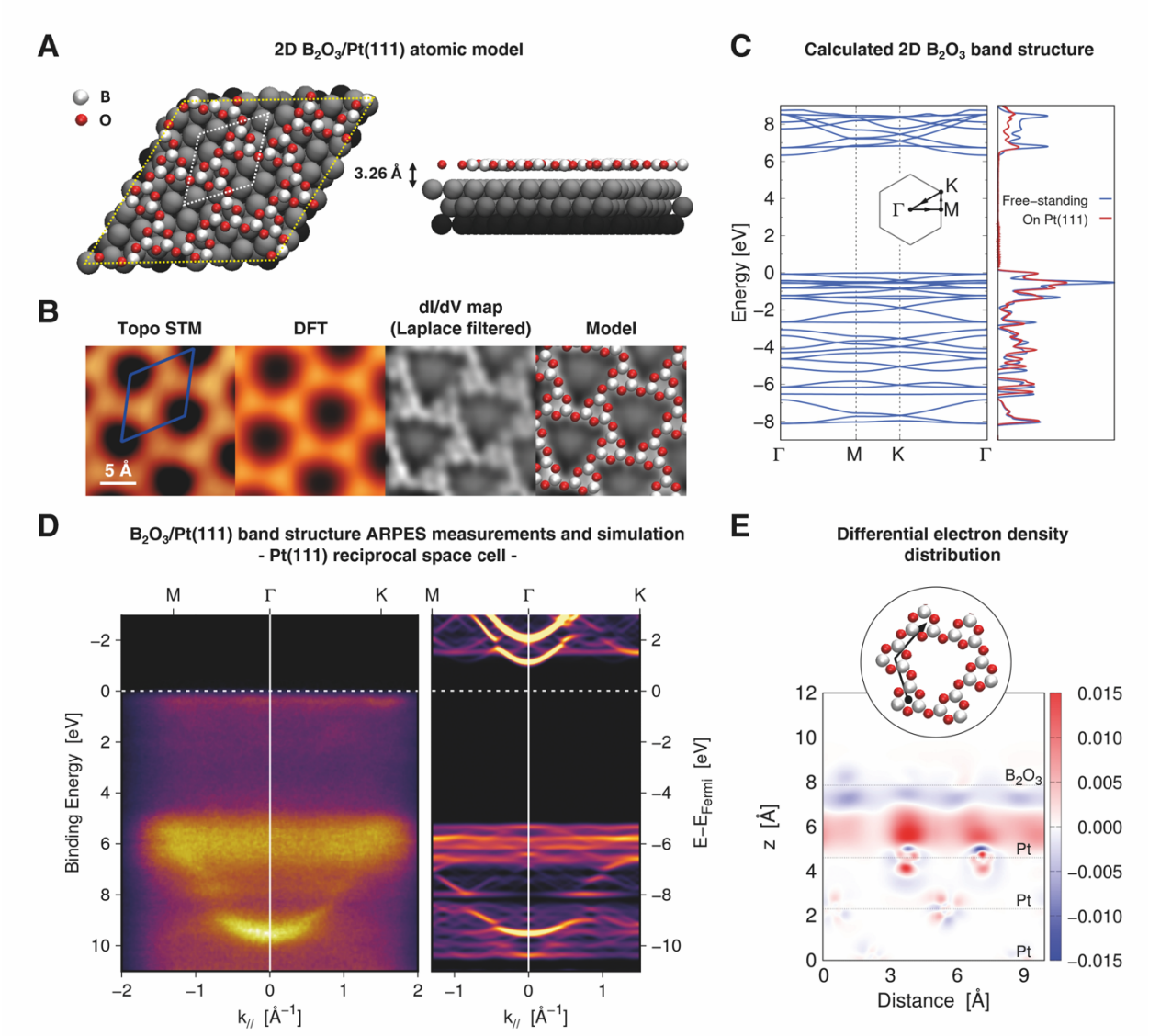

Fig. 3: **DFT calculation and experimental band structure of B_2O_3/Pt(111).** (**A**) Top and side views of the relaxed B_2O_3/Pt(111) system. The yellow and white dashed lines indicate the supercell of the entire system and the unit cell of the boria layer, respectively. The calculated average distance of 2D boria from the substrate is indicated. (**B**) From left to right, comparison of STM topographic image, simulated STM image, dI/dV conductance map and relaxed atomic model superposed to dI/dV map. The 2D unit cell of the boria layer is indicated in blue. The dI/dV map have been Laplace filtered to enhance the local contrast (+0.015 V, voltage modulation V_{AC} = 30 mV at 983 Hz and Δz = -0.23 nm. Δz is given with respect to opening the feedback loop at an STM set point of V = 1.0 V, I = 0.3 nA) and shows oxygen atoms as bright protrusions. (**C**) Calculated band structure of the optimized freestanding, flexible B_2O_3 model

along its high-symmetry axes. The zero energy is set to the highest occupied B_2O_3 electronic state. The right panel compares the Projected Density of States of the freestanding B_2O_3 and of the B_2O_3/Pt(111) system. (**D**) Momentum distribution curve of B_2O_3/Pt(111) extracted from ARPES data (p-polarization, photon energy 40 eV) along the high-symmetry axes of Pt(111) FBZ (left) and calculated band structure of free-standing B_2O_3 unfolded into the same FBZ (right). (**E)** Differential electron density distribution between the whole B_2O_3/Pt(111) system and its two constituents evaluated at different vertical positions while moving along the black line in the circular inlay. The numbers on the color scale are given in electrons per $Å^3$.